frontiers | Frontiers in Earth Science

TYPE Original Research
PUBLISHED 09 September 2025
DOI 10.3389/feart.2025.1659387

OPEN ACCESS

EDITED BY
Leilei Zhang,
Rice University, United States

REVIEWED BY
Zhengzheng Cao,
Henan Polytechnic University, China
Xiaojun Wu,
Changzhou University, China
Kun Qian,
Changzhou University, China
Zongxiao Ren,
Xi'an Shiyou University, China
Dongfeng Zhao,
School of Food and Pharmacy, Zhejiang Ocean University, China

*CORRESPONDENCE
Boying Li,
2022310159@student.cup.edu.cn

RECEIVED 04 July 2025
ACCEPTED 19 August 2025
PUBLISHED 09 September 2025

CITATION
Yang Y, Li B, Wang X, Qi M and Zhai D (2025) The research on intelligent evaluation methods for non-sealing faults in reservoirs based on well test analysis.
Front. Earth Sci. 13:1659387.
doi: 10.3389/feart.2025.1659387

The research on intelligent evaluation methods for non-sealing faults in reservoirs based on well test analysis

Yiyi Yang[1], Boying Li[2]*, Xudong Wang[1], Mingming Qi[1] and Di Zhai[1]

[1]CNOOC International Limited, Beijing, China, [2]College of Petroleum Engineering, China University of Petroleum, Beijing, China

In practical reservoirs, there exist a large number of non-sealing faults with flow capacity, which significantly influence oilfield development patterns and wellbore pressure transient behavior. The quantitative evaluation of fault sealing capacity is of great importance for characterizing remaining oil distribution and reconstructing flow fields. However, existing fault analysis methods are primarily qualitative, with limitations in the quantitative characterization of fault sealing. Traditional numerical well-test interpretation models do not account for fluid flow within faults, leading to significant deviations in well-test data interpretation, increased model-solving difficulties, and challenges in achieving quantitative analysis of reservoir sealing. Therefore, based on the fault, fluid, and reservoir property characteristics of the *X* reservoir, this study establishes a composite reservoir well-test interpretation mathematical model considering skin effects and solves the model using the Boltzmann transformation. By applying the "partial" mirror superposition principle, the dynamic response characteristics of typical curves under different fault boundary conditions are analyzed, and a quantitative sealing evaluation method suitable for non-sealing faults is developed. Furthermore, by integrating XGBoost multi-output regression and PSO algorithms, an intelligent hybrid inversion framework for identifying non-sealing faults in composite reservoirs is constructed: the XGBoost model predicts initial fault characteristic parameters, while the PSO algorithm performs global optimization to refine XGBoost parameters, ultimately inverting the fault connectivity coefficient (C_{fD}) and effective connected thickness (h_b). The results indicate the presence of a non-sealing fault *F1* between Well B30Y and Well B1A, with inverted values of $C_{fD} = 0.73$ and $h_b = 20.44$, demonstrating strong fault connectivity. Additionally, the fitting trend of bottom-hole flowing pressure during shut-in periods in both wells verifies the validity and stability of the proposed model. The method presented in this study enables rapid, quantitative, and precise evaluation of non-sealing fault closure, providing robust technical support for subsequent remaining oil potential exploitation and development strategy optimization.

KEYWORDS

non-sealing fault, well test analysis, intelligent evaluation, Boltzmann transformation, "partial" image method

1 Introduction

Currently, research on sealing faults is relatively mature both domestically and internationally, whereas studies on non-sealing faults with certain conductivity are comparatively limited. In actual reservoirs, the majority of faults possess a certain degree of conductivity, necessitating consideration of factors such as fault sealing capacity, conductivity, and connectivity. Consequently, for well test data from composite reservoirs with non-sealing faults, the well test interpretation models designed for sealing faults are not applicable, and the results obtained from such interpretations are often unreasonable (Liu et al., 2016; Zeng et al., 2017; Xing et al., 2023; Ma, 2025).

The theories of mirror image and potential function is a classical theoretical method employed to address reservoir engineering challenges (Dake, 1978; Liu et al., 2017). A quintessential application of the mirror image in reservoir engineering is the determination of the distance from a test well to nearby fault utilizing pressure drawdown or buildup well test data. However, the traditional mirror image method has only investigated the scenario of sealed faults without fluid flow, where the slope of the well test curve in semi-logarithmic coordinates exhibits an integer or specific multiple change upon encountering a fault; the D. R. Horner semi-logarithmic curve method (Horner, 1951) is commonly used to identify sealed faults. Prasad (1975) extended the model of a single sealed fault to include multiple intersecting or parallel sealed faults.

However, in actual reservoirs, particularly for faults within the reservoir where the fault displacement is less than the thickness of the reservoir formation, the majority are non-sealing faults with a certain degree of conductivity (Fu et al., 2022; Zhang, 2025; Fu et al., 2024; Hu et al., 2024; Liu et al., 2024; Li et al., 2023; Wang and Zhang, 1993). These cannot be effectively interpreted using well test models designed for sealing faults. For non-sealing faults, Bixel et al. (1963) were the first to propose treating the fault as a non-sealing boundary, but the model they established only considered the scenario where the properties of the rock and fluid change abruptly in the plane; Kuchuk and Tarek (1997) further refined the solution method for this model. Building upon the research of Stewart et al. (1984) and Streltsova and McKinley (1984) utilized numerical simulation to investigate the impact of partially communicating faults on interference well testing. Yaxely (1987) derived an analytical model for an infinite homogeneous reservoir containing a partially communicating fault; Abdelaziz and Tiab (2004) expanded on the work of L. M. Yaxley to study the pressure transient behavior in a homogeneous reservoir with two intersecting fault boundaries. The existing physical models of non-sealing faults only consider the different fluid properties within the reservoir, while the flow of fluids within the fault itself has not been studied.

Meanwhile, most current intelligent well-test interpretation and inversion models fail to account for the presence of non-sealing faults in the reservoir. Li (2023) developed an automated well-test interpretation method based on convolutional neural networks (CNN), enabling the input of complete pressure derivative curves as variables and overcoming the limitations of traditional automatic matching approaches that rely on parameter optimization algorithms. Dong and Liao (2023) proposed an automated well-test interpretation method combining the Deep Deterministic Policy Gradient (DDPG) algorithm with a Long Short-Term Memory (LSTM) surrogate model, achieving efficient automatic curve matching under four distinct well-test model conditions. Mi et al. (2021) constructed a multi-modal stochastic analysis well-test interpretation model integrating model parameters and curves, employing ensemble Kalman filtering for well-test curve matching, thereby enhancing the interpretation of complex flow regimes and boundary effects. Li et al. (2020) introduced a CNN-based automated well-test interpretation method for radial composite reservoirs, realizing automatic parameter matching in such reservoirs.

Based on the fault, fluid, and reservoir properties of the *X* reservoir, this study establishes a mathematical model for well-test interpretation in composite reservoirs, which is solved using Boltzmann transformation. By applying the "partial" image superposition principle, we analyze the dynamic response characteristics of type curves under different fault boundary conditions. Furthermore, an inversion framework for non-sealing fault parameters in composite reservoirs is developed by integrating this model with eXtreme Gradient Boosting (XGBoost) multi-output regression and particle swarm optimization (PSO) algorithm, enabling efficient and accurate identification of fault characteristics.

2 Construction and intelligent solution of well test models for non-sealing faults

2.1 Establishment of well testing model for non-sealing faults

In an infinite homogeneous reservoir, the presence of a partially permeable fault with certain flow capacity is considered, where both sides of the fault exhibit partial conductivity. The physical model is illustrated in Figure 1. Well A is located at a distance d from fault F, and well A′ is a "mirror image" reflection well with respect to the fault plane F. Assuming the production rate of well A is q_A, to simulate the scenario where fluid flows across the fault, the production rate of the "mirror image" well A′ is assumed to be: αq_A. Here, α represents the degree of completeness of the mirror reflection. In an infinite homogeneous reservoir, the presence of a partially permeable fault with certain flow capacity is considered, where both sides of the fault exhibit partial conductivity. The physical model is illustrated in Figure 1. Well A is located at a distance d from fault F, and well A′ is a "mirror image" reflection well with respect to the fault plane *F*. Assuming the production rate of well A is q_A, to simulate the scenario where fluid flows across the fault, the production rate of the "mirror image" well A′ is assumed to be: αq_A. Here, α represents the degree of completeness of the mirror reflection. As shown in Figure 1, the reservoir is divided into an inner zone (Region 1) and an outer zone (Region 2), with distinct properties such as permeability, porosity, and fluid characteristics (i.e., a radial composite reservoir model). The outer zone contains a non-sealing boundary (i.e., a conductive fault), modeled as a linear conductive boundary. For simplification, this boundary is assumed to be located in the outer zone at a distance *L* from well A (representing a 1D radial flow boundary response).

Similar to homogeneous and dual-porosity reservoirs, when interpreting well test data from composite oil and gas reservoirs

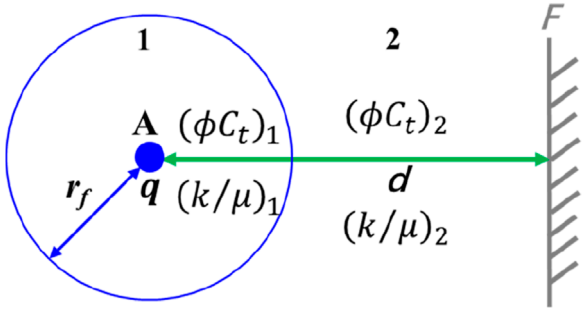

FIGURE 1
Schematic diagram of mirror image reflection in a homogeneous reservoir.

with faults, the pressure derivative curve of the test data can become highly complex due to the presence of faults, affecting the mid- and late-time behavior of the curve. Therefore, the influence of faults on the characteristic well test model response of composite reservoirs can be analyzed by applying the partial image method and the superposition principle.

The model assumptions are as follows:

1. Both the inner and outer zones exhibit homogeneous, isothermal, single-phase fluid flow, with gravity and capillary forces neglected.
2. The well is located at the center of the inner zone (r = 0), producing at a constant rate (q). Wellbore storage effects (storage coefficient: C) and skin effects (skin factor: S) are considered.
3. The non-sealing boundary satisfies the conductive boundary condition: pressure continuity across the boundary; Flow rate proportional to the pressure difference between inner and outer zones (representing cross-boundary fluid transfer capacity)

Based on the assumptions, applying the theory of fluid flow mechanics, the model for well testing in a homogeneous reservoir is established:

Based on flow theory in porous media, the following mathematical model can be established:

1. Inner zone ($0 < r < r_f$) Equations:

$$\frac{1}{r}\frac{\partial}{\partial r}\left(rk_1\frac{\partial p_1}{\partial r}\right) = \phi_1\mu_1 C_{t1}\frac{\partial p_1}{3.6\partial t} \tag{1}$$

Where, k_1: inner zone permeability, md; ϕ_1: inner zone porosity; C_{t1}: inner zone total compressibility, MPa^{-1}; p_1: inner zone pressure, MPa; μ_1: inner zone fluid viscosity, mPa·s.

2. Outer zone ($r > r_f$) Equations:

$$\frac{1}{r}\frac{\partial}{\partial r}\left(rk_2\frac{\partial P_2}{\partial r}\right) = \phi_2\mu_2 C_{t2}\frac{\partial P_2}{3.6\partial t} \tag{2}$$

Where, k_2: outer zone permeability, md; ϕ_2: outer zone porosity; C_{t2}: outer zone total compressibility, MPa^{-1}; p_2: outer zone pressure, MPa; μ_2: outer zone fluid viscosity, mPa·s.

3. Inner-outer zone interface conditions:

Pressure and flow rate continuity across the interface are governed by:

$$P_1(r_f,t) = P_2(r_f,t) \tag{3}$$

$$\frac{k_1}{\mu_1}\frac{\partial P_1}{\partial r}|_{r=r_f} = \frac{k_2}{\mu_2}\frac{\partial P_2}{\partial r}|_{r=r_f} \tag{4}$$

4. Non-sealing boundary conditions (outer zone boundary: $r = d$):

$$\frac{k_2 h}{\mu_2}\frac{\partial P_2}{\partial r}\Big|_{r=d} = \frac{k_b \acute{h}_b}{\mu_2}(P_2 - P_i) \tag{5}$$

Where, $\frac{k_b\acute{h}_b}{\mu_2}$: conductivity of the non-sealing boundary (C_F); P_i: initial reservoir pressure, MPa.

5. Wellbore conditions and initial conditions

Accounting for wellbore storage and skin effects, the wellbore boundary condition is expressed as:

$$C\frac{dp_w}{dt} = qB - 172.8\pi r_w k_1 h\frac{\partial p_1}{\partial r}|_{r=r_w} \tag{6}$$

$$P_w(t) = P_1(r_w,t) + \frac{172.8\pi q\mu_1 B}{k_1 h}S \tag{7}$$

Where, h: net pay thickness, m; B: formation volume factor; q: surface production rate, m^3/d.

The initial reservoir condition is defined as:

$$P_1(r,0) = P_2(r,0) = P_i \tag{8}$$

2.2 Solution methodology for non-sealing fault well testing model (laplace transform approach)

1. Dimensionless transformation

The dimensionless parameters are defined as shown in Equations 9–17.

$$P_{D1} = \frac{k_1 h}{172.8\pi q\mu B}(P_i - P_1) \tag{9}$$

$$P_{D2} = \frac{k_2 h}{172.8\pi q\mu B}(P_i - P_2) \tag{10}$$

$$t_D = \frac{3.6k_1}{\phi_1\mu C_{t1} r_w^2}t \tag{11}$$

$$r_D = \frac{r}{r_w} \tag{12}$$

$$r_{fD} = \frac{r_f}{r_w} \tag{13}$$

$$d_D = \frac{d}{r_w} \tag{14}$$

$$C_D = \frac{2\pi}{\phi_1 \mu C_{t1} r_w^2} C \tag{15}$$

$$\omega = \frac{k_1 \phi_2 \mu_2 C_{t2}}{k_2 \phi_1 \mu_1 C_{t1}} \tag{16}$$

$$C_{fD} = \frac{k_b h_b r_w}{k_2 h L_b} \tag{17}$$

Where, C_D: dimensionless storage coefficient; C: storage coefficient, m^3/MPa; C_{fD}: fault connectivity coefficient; k_b: fault zone permeability, mD; h_b: effective connected thickness of the fault: m; ω: storativity ratio between inner and outer zones; C_{t1}, C_{t2}: total compressibility of the inner zone and outer zone, MPa^{-1}.

Equation 16 characterizes the flow capacity contrast between the two zones, and Equation 17 represents the dimensionless conductivity of the boundary. By applying dimensionless transformation to Equations 1–8. We obtain Equations 18–24:

$$\frac{1}{r_D}\frac{\partial}{\partial r_D}\left(r_D \frac{\partial P_{1D}}{\partial r_D}\right) = \frac{\partial P_{1D}}{\partial t_D} \tag{18}$$

$$\frac{1}{r_D}\frac{\partial}{\partial r_D}\left(r_D \frac{\partial P_{2D}}{\partial r_D}\right) = \omega \frac{\partial P_{2D}}{\partial t_D} \tag{19}$$

$$P_{1D}\left(r_{fD}, t_D\right) = P_{2D}\left(r_{fD}, t_D\right) \tag{20}$$

$$\left.\frac{\partial P_{1D}}{\partial r_D}\right|_{r_D = r_{fD}} = \left.\frac{\partial P_{2D}}{\partial r_D}\right|_{r_D = r_{fD}} \tag{21}$$

$$\left.\frac{\partial P_{2D}}{\partial r_D}\right|_{r_D = d_D} = C_{fD} P_{2D} \tag{22}$$

$$C_D \frac{dP_{WD}}{dt_D} = 1 - \left.\frac{\partial P_{1D}}{\partial r_D}\right|_{r_D = 1} \tag{23}$$

$$P_{WD}(t_D) = \left(P_{1D} - S\frac{\partial P_{1D}}{\partial r_D}\right)|_{r_D = 1} \tag{24}$$

2. Solution in Laplace Domain

By applying the Laplace transform to Equations 18–22, the solutions for the inner and outer zones are obtained.

Inner zone solution:

$$\overline{P_{1D}}(S) = \frac{1}{S}\left[K_0\left(\sqrt{S} r_D\right) + \frac{S}{\sqrt{S}}\right] + \frac{C_D \sqrt{S}}{S}\left[\sqrt{S}\overline{P_{1D}}(S) - \frac{\partial \overline{P_{1D}}}{\partial r_D}|_{r_D = 1}\right] \tag{25}$$

Outer zone solution:

$$\overline{P_{2D}}(S) = \overline{P_{1D}}(S)|_{r_D = r_{fD}} = \frac{K_0\left(\sqrt{\omega S} r_D / r_{fD}\right) + \frac{C_{fD}\sqrt{\omega S} K_1\left(\sqrt{\omega S} r_D / r_{fD}\right)}{1 + C_{fD}\sqrt{\omega S} K_1\left(\sqrt{\omega S} r_D / r_{fD}\right)}}{K_0 \sqrt{\omega S}} \tag{26}$$

2.3 Discussion on the solution of the non-sealing fault well test model

According to the law of images in seepage mechanics, the partial "image" reflection method is applied. Let α represent the degree of completeness of the image reflection. When $\alpha = 0$, it reflects the scenario where the fault conductivity is entirely equal to the reservoir conductivity; when $\alpha = 1$, it reflects the scenario where the fault is completely sealing; and when $0 < \alpha < 1$, it reflects the scenario of partial fault conductivity. After reflection, the fault disappears, and the pressure decline behavior of the original well is then solved using the superposition principle.

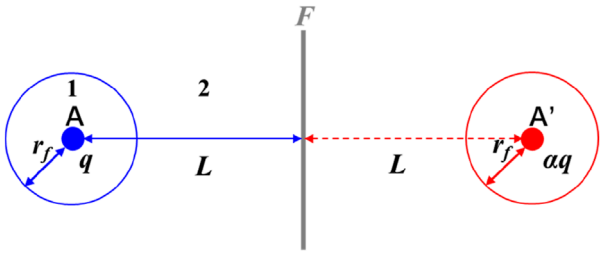

FIGURE 2
Composite reservoir mirror image method schematic diagram.

As shown in Figure 2, Well A is located in a two-zone composite reservoir, where the inner zone (Region 1) is near the wellbore, and the outer zone (Region 2) extends farther away. Well A is positioned at a distance d from Fault F. Well A′ is a "mirror image" reflection well generated with respect to the fault plane F. Assuming Well A produces at a rate q, to simulate fluid flow across the fault, the production rate of the "mirror image" well A′ is set as $q' = \alpha q$, where α represents the degree of completeness of the mirror reflection.

Let $\eta_1 = \frac{k_1}{(\varphi \mu C_t)_1}$, $\eta_2 = \frac{k_2}{(\varphi \mu C_t)_2}$, $M_{12} = \frac{(k/\mu)_1}{(k/\mu)_2}$,the bottomhole pressure drop of the well A at time t after opening the well is:

$$\begin{aligned}\Delta P = P_i - P_{wf} = \frac{q\mu_1 B}{345.6\pi k_1 h}\left\{-Ei\left(-\frac{r_w^2}{14.4\eta_1 t}\right) + Ei\left(-\frac{r_f^2}{14.4\eta_1 t}\right)\right. \\ \left. - M_{12} Ei\left(-\frac{r_f^2}{14.4\eta_1 t}\right)\exp\left[-\frac{r_f^2}{14.4\eta_1\eta_2 t}(\eta_2 - \eta_1)\right]\right\} \\ + \frac{aq\mu_2 B}{345.6\pi k_2 h}\left\{-Ei\left(-\frac{(2d)^2}{14.4\eta_2 t}\right)\exp\left[-\frac{r_f^2}{14.4\eta_1\eta_2 t}(\eta_2 - \eta_1)\right]\right\}\end{aligned} \tag{27}$$

In Equation 27, the first term on the right-hand side represents the pressure drawdown at the wellbore induced by fluid flow from the near-well formation (Region 1), the second term corresponds to the pressure response from the distant formation (Region 2), while the third term characterizes the pressure interference caused by the image well (A′). During the early-time period before the pressure transient reaches the boundary of region 1 ($t < t_1$), the contributions of both the second and third terms become negligible. By applying the logarithmic approximation to the exponential integral function *-Ei(-x)* and incorporating skin effects, Equation 27 can be simplified to Equation 28:

$$\begin{aligned}P_{wf} &= P_i - \frac{2.12 \times 10^{-3} q\mu_1 B}{k_1 h}\left[\lg t + \lg\left(\frac{\eta_1}{r_w^2}\right) + 0.9077 + 0.8686S\right] \\ &= P_i - m_1\left[\lg t + \lg\left(\frac{\eta_1}{r_w^2}\right) + 0.9077 + 0.8686S\right]\end{aligned} \tag{28}$$

Where, P_{wf}: bottom hole Pressure, MPa.

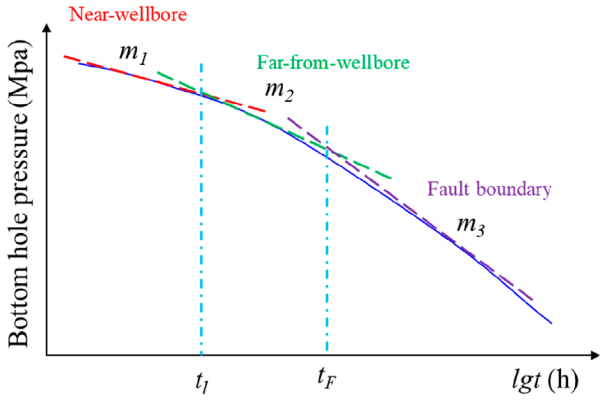

FIGURE 3
Schematic diagram of semi-logarithmic well test curve showing bottomhole pressure variation over time.

As shown in Figure 3, plotting the semi-logarithmic relationship between P_{wf} and lgt yields a straight-line segment with a slope of m_1, where the expression for m_1 is shown in Equation 29:

$$m_1 = \frac{2.12\times10^{-3}q\mu_1 B}{k_1 h} \tag{29}$$

When the pressure drawdown from the producing well has propagated to the boundary of region 1 but before the pressure disturbance from the image well reaches the producing well (i.e., during the time period $t < t_F$), the third term in Equation 27 becomes negligible. By approximating the exponential integral function *-Ei(-x)* with its logarithmic equivalent and incorporating skin effects, Equation 27 can be simplified to Equation 30:

$$\begin{aligned} P_{wf} &= P_i - \frac{2.12\times10^{-3}q\mu_2 B}{k_2 h}\left[\lg t + \frac{2}{M_{12}}\lg\left(\frac{r_f}{r_w}\right) + \lg\left(\frac{\eta_2}{r_f^2}\right) + 0.9077 + 0.8686S\right] \\ &= P_i - m_2\left[\lg t + \frac{2}{M_{12}}\lg\left(\frac{r_f}{r_w}\right) + \lg\left(\frac{\eta_2}{r_f^2}\right) + 0.9077 + 0.8686S\right] \end{aligned} \tag{30}$$

As shown in Figure 3, plotting the semi-logarithmic relationship between P_{wf} and lgt yields a straight-line segment with a slope of m_2. The expression for m_2 can be represented by Equation 31:

$$m_2 = \frac{2.12\times10^{-3}q\mu_2 B}{k_2 h} \tag{31}$$

As illustrated in Figure 3, m_1, m_2, and m_3 correspond to the slopes of the straight-line segments in the semi-log plot, reflecting the pressure depletion rates during different flow regimes. These slope values quantitatively characterize the flow capacity of fluids passing through distinct reservoir regions: m_1: near-wellbore zone; m_2: outer reservoir region; m_3: fault boundary zone. In this study, we focus on evaluating the flow conductivity near the fault based on this methodology. Thus, special emphasis is placed on the analysis of m_2 and m_3, which are critical for assessing. The bottom-hole flowing pressure is shown in Equation 32:

$$\begin{aligned} P_{wf} &= P_i - \frac{2.12\times10^{-3}q\mu_2 B}{k_2 h}\left[\lg t + \frac{2}{M_{12}}\lg\left(\frac{r_f}{r_w}\right) + \lg\left(\frac{\eta_2}{r_f^2}\right) + 0.9077 + 0.8686S\right] \\ &\quad - \frac{2.12\times10^{-3}\alpha q\mu_2 B}{k_2 h}\left[\lg t + \frac{2}{M_{12}}\lg\left(\frac{d}{r_f}\right) + \lg\left(\frac{\eta_2}{d^2}\right) + 0.3056\right] \\ &= P_i - m_3\lg t - m_2\left[\frac{2}{M_{12}}\lg\left(\frac{r_f}{r_w}\right) + \lg\left(\frac{\eta_2}{r_f^2}\right) + 0.9077 + 0.8686S\right] \\ &\quad - \alpha m_2\left[\frac{2}{M_{12}}\lg\left(\frac{d}{r_f}\right) + \lg\left(\frac{\eta_2}{d^2}\right) + 0.3056\right] \end{aligned} \tag{32}$$

As shown in Figure 3, plotting the semi-logarithmic relationship between P_{wf} and lgt yields a straight-line segment with a slope of m_3. Where the expression for m_3 can be represented by Equation 33:

$$m_3 = \frac{2.12\times10^{-3}(1+\alpha)q\mu_2 B}{k_2 h} = (1+\alpha)m_2 \tag{33}$$

Where the expression for a can be represented by Equation 34:

$$\alpha = \frac{m_3}{m_2} - 1 \tag{34}$$

When $\alpha = 1$, $m_3 = 2m_2$, indicating a completely sealed fault condition where no fluid flows across the fault; when $\alpha = 0$, $m_3 = m_2$, reflecting that the fault's flow conductivity is exactly equal to the reservoir's flow conductivity, meaning fluid can completely pass through the fault; when $0 < \alpha < 1$, the relationship between m_3 and m_2 is non-integer, representing partial flow conductivity of the fault, which shows that the fault partially blocks fluid flow.

3 Analysis of pressure response characteristics in well testing models for non-sealing faults

The Stehfest numerical inversion algorithm was applied to Equations 25, 26 to obtain the time-domain solution of dimensionless bottomhole pressure, from which the dimensionless pressure derivative was calculated. Equation 35 presents the Stehfest Laplace numerical inversion algorithm. Subsequently, the characteristic response curves of the non-sealing fault well-testing model were generated, as illustrated in Figures 4, 5.

$$p_{wD}(t) = \frac{\ln 2}{t}\sum_{i=1}^{M}\lambda_i\bar{p}_{wD}(u_i)u_i = (\ln 2/t)i\lambda_i = (-1)^{i+M/2}\sum_{k=(i+1)/2}^{\min(i,M/2)}\left[k^{M/2}(2k)!\right]/ \\ [(M/2-k)!\times k!(k-1)!(i-k)!(2k-i)!] \tag{35}$$

Where, p_{wD}: the dimensionless bottomhole pressure in Laplace space, MPa; z: the Laplace variable.

The well-testing curves (pressure and pressure derivative) for non-sealing faults can be divided into four characteristic stages:

1. Early-time wellbore storage and skin-dominated flow regime: The dimensionless pressure derivative curve initially exhibits a unit-slope straight line (indicating wellbore storage dominance); Subsequently transitions to an upward-convex curve (reflecting skin effects)

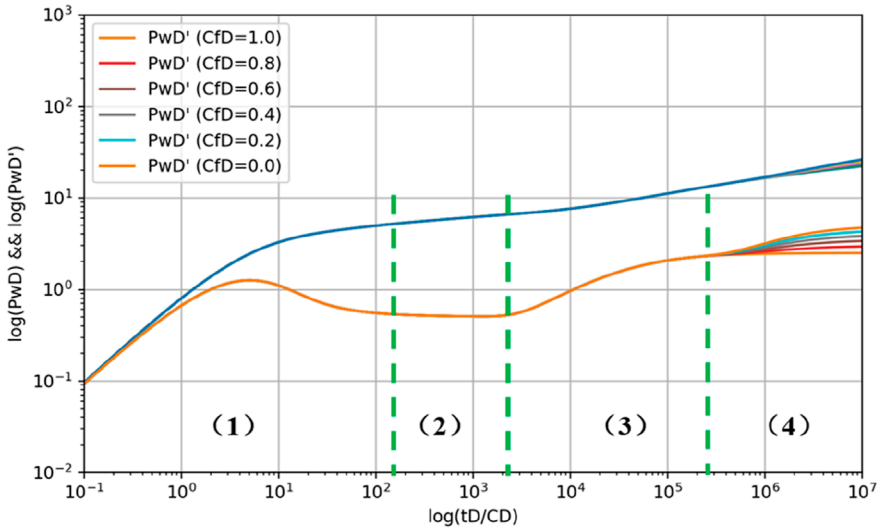

FIGURE 4
Characteristic well test response curves of composite reservoirs under various non-sealing fault conditions (outer zone mobility < inner zone mobility).

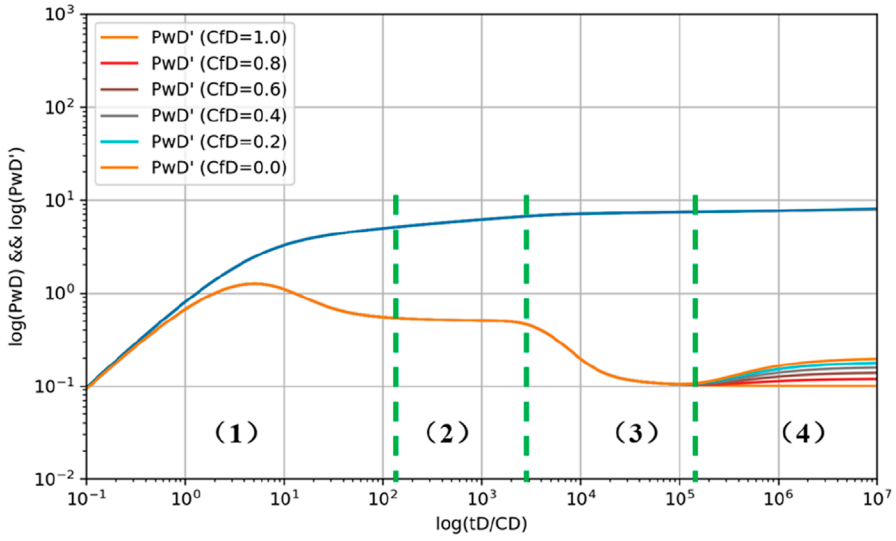

FIGURE 5
Characteristic well test response curves of composite reservoirs under various non-sealing fault conditions (outer zone mobility > inner zone mobility).

2. Mid-time radial flow regime: the dimensionless pressure derivative curve stabilizes into a horizontal line with zero slope (approaching 0.5); Demonstrates formation fluid flowing radially toward the wellbore
3. Transitional Response Phase: this stage reflects the flow transition from the inner zone to the outer zone in the composite reservoir system. When outer zone mobility is lower than inner zone mobility: the dimensionless pressure derivative curve initially exhibits an upward deflection, subsequently entering a stabilized pseudo-radial flow regime (Figure 4). When outer zone mobility exceeds inner zone mobility: the derivative curve first shows a "dip", then stabilizes into pseudo-radial flow (Figure 5).
4. In the late outer boundary response stage, the characteristic curve of the dimensionless pressure derivative is affected by the mobility contrast between the outer and inner zone and the fault sealing parameter (C_{fD}). When the mobility in the outer zone is smaller than that in the inner zone, as shown in Figure 4: when the outer boundary is a fully connected fault ($C_{fD} = 1.0$), the characteristic curve is a horizontal line with the value of $0.5\frac{k_1\mu_2}{k_2\mu_1}$; the curve of the fully sealing fault ($C_{fD} = 0.0$) is upwardly curved first, and finally stabilized at the horizontal line with the value of $\frac{k_1\mu_2}{k_2\mu_1}$; the curve of the non-sealing fault ($0.0 < C_{fD} < 1.0$) has a similar shape, which is upwardly curved first and then stabilized with the stabilized value between the two previous ones. On the contrary, as shown in Figure 5, when

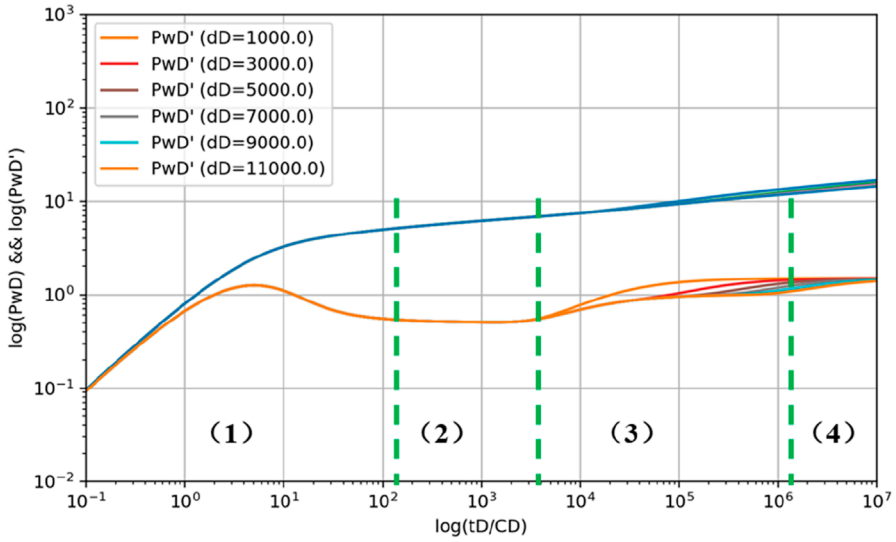

FIGURE 6
Characteristic well test response curves of composite reservoirs under varying boundary distances (outer zone mobility < inner zone mobility).

the flow in the outer zone is larger than that in the inner zone, the curve characteristic law is consistent with the above case. The characteristic curves of unconfined faults, which are 'upturned and then stabilized, and the stabilization value is in the middle', are the core markers that distinguish them from the confined faults.

Figures 6, 7 display the characteristic response curves of the non-sealing fault well-test model under varying boundary distances. Analytical results demonstrate that for both cases where outer zone mobility is either lower or higher than inner zone mobility, the onset time of dimensionless pressure derivative increase shows a significant positive correlation with boundary distance. Specifically, as the boundary distance progressively increases, the initiation point of the dimensionless pressure derivative rise exhibits a clearly delayed trend.

4 Intelligent evaluation methodology for fault sealing capacity

As previously discussed, for reservoirs incorporating an image well within a Cartesian coordinate system (Figure 8), the formation pressure $P_2(t)$ at any arbitrary point M (x, y) when $t > t_f$ can be mathematically represented by Equation 36:

$$P_2(t) = P_i - \frac{2.12\times10^{-3}q\mu_1 B}{k_1 h}\left\{\lg\left(\frac{14.4\eta_1 t}{\gamma[(x+d)^2+y^2]}\right) - \lg\left(\frac{14.4\eta_1 t}{\gamma r_f^2}\right) + M_{12}\lg\left(\frac{14.4\eta_1 t}{\gamma r_f^2}\right)\exp\left[-\frac{r_f^2}{14.4\eta_1\eta_2 t}(\eta_2-\eta_2)\right] + 0.8686S\right\} - \alpha\frac{2.12\times10^{-3}q\mu_2 B}{k_2 h}\left\{\lg\left(\frac{14.4\eta_2 t}{\gamma(x-d)^2+y^2]}\right)\exp\left[-\frac{r_f^2}{14.4\eta_1\eta_2 t}(\eta_2-\eta_2)\right]\right\} \quad (36)$$

The derivative of Equation 35 in the x-direction can be expressed by Equation 37:

$$\frac{\partial P_2(t)}{\partial x} = -\frac{1.842\times10^{-3}q\mu_1 B}{k_1 h}\left[\frac{x+d}{(x+d)^2+y^2} + \frac{\alpha M_{12}(x-d)}{(x-d)^2+y^2}\exp\left(-\frac{r_f^2}{14.4\eta_1\eta_2 t}(\eta_2-\eta_1)\right)\right] \quad (37)$$

Thus, the pressure gradient at the location of the fault plane, i.e., on the y-axis, is expressed by Equation 38.

$$\left.\frac{\partial P_2(t)}{\partial x}\right|_{x=0} = -\frac{1.842\times10^{-3}q\mu_1 B}{k_1 h}\times\left[\frac{d}{d^2+y^2} - \frac{\alpha M_{12}d}{d^2+y^2}\exp\left(-\frac{r_f^2}{14.4\eta_1\eta_2 t}(\eta_2-\eta_1)\right)\right] \quad (38)$$

The flow rate across a unit length fault at any instant is expressed by Equation 39:

$$q_F = \frac{k_2 h}{\mu_2}\left.\frac{\partial P_2(t)}{\partial x}\right|_{x=0} = -\frac{1.842\times10^{-3}q\mu_2 BC_f d}{k_2 h(d^2+y^2)}\times\left[1-\alpha M_{12}\exp\left(-\frac{r_f^2}{14.4\eta_1\eta_2 t}(\eta_2-\eta_1)\right)\right] \quad (39)$$

Where, C_f is the conductivity of the reservoir, i.e., is the conduction coefficient or is the flow coefficient $(k_1 h/\mu_1)$.

The conductivity of the fault, denoted as C_F, satisfies Equation 40:

$$C_F = \left[1-\alpha M_{12}\exp\left(-\frac{r_f^2}{14.4\eta_1\eta_2 t}(\eta_2-\eta_1)\right)\right]C_f \quad (40)$$

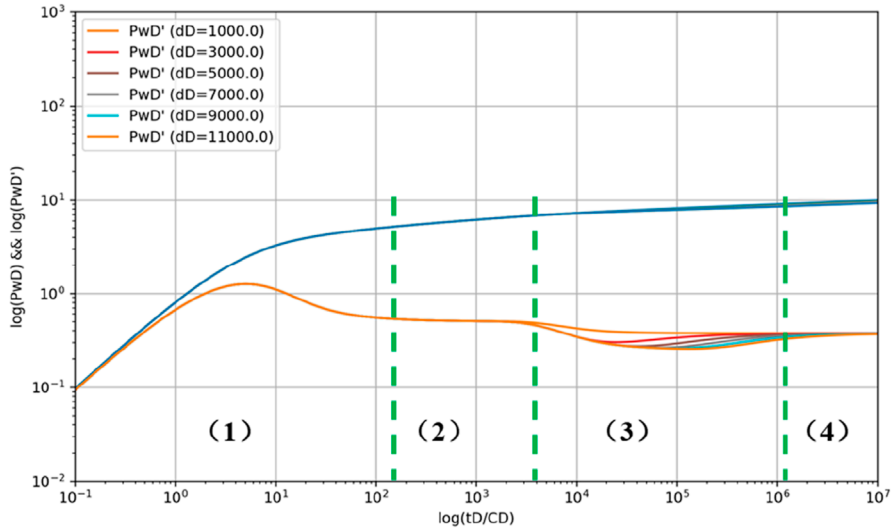

FIGURE 7
Characteristic well test response curves of composite reservoirs under varying boundary distances (outer zone mobility > inner zone mobility).

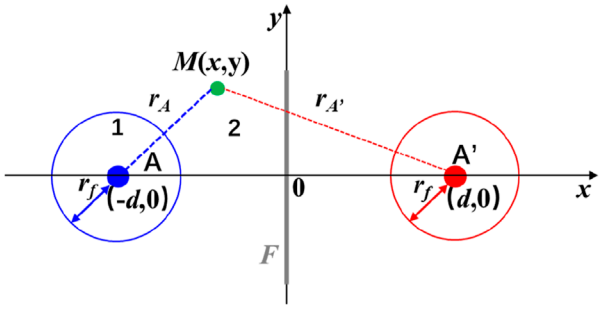

FIGURE 8
Schematic diagram of composite reservoir Configuration and well locations in cartesian coordinates.

Substituting Equation 33 into Equation 40 yields Equation 41:

$$C_F = \left[2 - \frac{m_3}{m_2}\right] C_f \tag{41}$$

There β can be expressed by Equation 42.

$$\beta = \frac{m_3}{m_2} \tag{42}$$

$$C_F = (2 - \beta) C_f \tag{43}$$

By determining the slope change magnification factor β from semi-log well test curves and substituting it into Equation 43, the fault conductivity or transmissibility across the fault can be obtained.

To quantitatively describe the observable connectivity between reservoir units achieved by fault conductivity, we define the effective fault thickness (h) as shown in Equation 44:

$$h_b = C_F \frac{\mu}{k_F} = (2 - \beta) C_f \frac{\mu}{k} = (2 - \beta) h \tag{44}$$

In order to express the degree of connectivity of the fault to the reservoir on both sides, the fault connectivity coefficient is defined by the following Equation 45:

$$C_{fD} = \frac{C_F}{C_f} = 2 - \beta \tag{45}$$

To achieve rapid and accurate inversion of key fault parameters under complex non-sealing fault well-testing conditions, this paper proposes an intelligent hybrid modeling workflow. Based on the mathematical model established in Section 2, a theoretical type curve database was first generated. After feature extraction and normalization preprocessing, the XGBoost algorithm was employed for multi-output regression prediction. The PSO algorithm was then introduced to perform global search and optimal configuration of hyperparameters. Building upon the characteristic response features of multi-stage flow regimes, K-fold cross-validation was applied to thoroughly validate and optimize the model performance, thereby enhancing the robustness and generalization capability of fault parameter identification.

1. Dataset establishment

Based on the previously developed composite non-sealing fault well-test interpretation mathematical model, a numerical simulation method was employed to generate type curve data samples to support machine learning training and validation.

Sample Size: a total of 1,000 synthetic pressure and derivative curves for composite reservoirs were generated, covering various combinations of fault and reservoir properties, including: inner and outer zone permeability: 100–1,000 mD; Porosity: 0.15–0.30; Mobility ratio: 0.5–2; Fault boundary distance: 1,000–10,000 m.

2. Data processing and feature extraction

To enhance the efficiency and stability of model training, preprocessing was performed on the simulated curves and reservoir properties:

a. Feature denoising: wavelet transform was applied to the simulated pressure derivative curves to eliminate numerical fluctuations and improve feature extraction accuracy.
b. Input Feature Extraction: for each type curve, the following input features were extracted:
   ① reservoir property parameters: inner and outer zone permeability, porosity, mobility ratio and fault boundary distance.
   ② Flow regime characteristics: based on pressure derivative response, the curves were divided into: wellbore storage effect, radial flow regime, transitional flow regime, outer boundary effect regime, critical time points (m_2, m_3) for regime transitions and duration of each flow stage.

To eliminate the influence of differing dimensions and numerical scales across parameters, a normalization approach was implemented. Permeability values first underwent logarithmic transformation followed by standardization (Z-score normalization) to normalize their distribution. The mobility ratio and fault boundary distance were scaled to the [0,1] interval using min-max normalization to maintain consistent value ranges. For time-dependent features including characteristic transition points (m_2, m_3) and flow regime durations, global min-max normalization was applied based on the extreme values observed across the entire dataset.

3. Dataset partitioning and cross-validation

To rigorously evaluate the model's generalization capability and prevent overfitting, this study employed 5-fold cross-validation (k = 5) for dataset partitioning and validation. The implementation process was as follows:

Random Partitioning: The type curve database was randomly divided into 5 equally sized subsets while maintaining data distribution consistency.

Iterative Training-Validation: in each iteration, 4 subsets were used as the training set, while the remaining 1 subset served as the validation set. This process was repeated until all 5 subsets had been used as the validation set exactly once. After completing all iterations, the average performance metrics across the 5 validation rounds were calculated to provide a comprehensive evaluation of the model's robustness.

4. XGBoost model and hyperparameter configuration

This study employed XGBoost as a multi-output regression model to establish the nonlinear mapping relationship between type curve characteristics and fault-related parameters (m_2, m_3). The Mean Squared Error (MSE) was adopted as the loss function to quantify and minimize the discrepancy between the model's predicted values and the actual target parameters (m_2, m_3).

5. PSO for hyperparameter tuning

To further enhance the generalization capability of the XGBoost model, this study employed the PSO algorithm for global search and automated optimization of key hyperparameters. The PSO implementation adopted the following configuration: A swarm of 30–50 particles was randomly initialized to explore the predefined parameter space. During each iteration, particle positions were dynamically updated based on both individual best and global best solutions, with the optimization process continuing until either fitness convergence or reaching the maximum iteration limit (50–100 cycles). The algorithm incorporated an inertia weight that linearly decayed from 0.9 to 0.4 and uniform learning factors ($c_1 = c_2$ = 1.5). The search space encompassed critical XGBoost parameters including: learning rate (0.01–0.2), maximum tree depth (4–8), and regularization parameters (L_1: 0–1, L_2: 0–2). This systematic approach balanced exploration and exploitation to identify optimal hyperparameter combinations that maximize model performance.

6. Optimal XGBoost model training and multi-target prediction

Upon obtaining the optimized hyperparameters, the XGBoost model was retrained using the complete training dataset while monitoring validation error to ensure optimal performance. The finalized model was then employed to conduct multi-target predictions on an independent test set, simultaneously outputting the critical parameters m_2 and m_3.

5 Application and analysis of fault seal evaluation in typical reservoirs

Faults are highly complex geological phenomena, and their conductivity is influenced by factors such as fracture stress, faulting mechanisms, fault orientation, types of minerals on the fault plane, and the distribution patterns of these minerals. No fault is absolutely sealing; each possesses a certain degree of conductivity, albeit varying in magnitude. While the location of a fault can be determined through seismic or other geological analysis methods and confirmed via well test analysis, the conductivity of a fault can only be determined through dynamic testing and analysis methods.

The *X* reservoir is located on the slope belt of the Grampian Arch, within a graben controlled by two NE-SW trending faults to the north and south. The oilfield features well-developed internal faults, including a set of NE-SW trending faults parallel to the graben and a contemporaneous set of NW-SE trending faults, forming a conjugate fault pattern. Planar distribution divides the oilfield into six fault blocks based on fault development characteristics from south to north. As shown in Figure 9: This displays a cross-section of the 3D fault-architecture model surrounding Well B1A, where Well B1A and Well B30Y are separated by Fault *F1*. The fault edges on both sides of *F1* exhibit sandstone-to-sandstone juxtaposition, with a throw smaller than the reservoir thickness (28 m), indicating partial connectivity across the fault zone.

To rapidly quantify the transmissibility of the non-sealing fault *F1*, a pre-established intelligent hybrid inversion framework was implemented to analyze the composite reservoir between wells B1A and B30Y.

Permeability and mobility data from wells B1A and B30Y, along with the estimated fault throw, were first standardized or normalized to enhance the model's stability and predictive accuracy. These processed parameters were then fed into a pretrained XGBoost multi-output regression model to obtain initial estimates of the key flow regime transition points, m_2 and m_3.

The initial predictions of m_2 and m_3 from the XGBoost model were subsequently used as the starting search centers for the Particle Swarm Optimization (PSO) algorithm. Taking the misfit between the measured pressure derivative curve and the simulated response

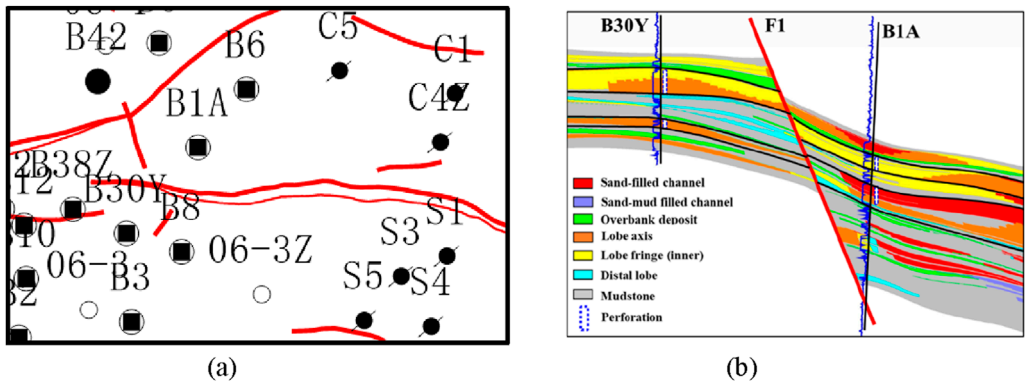

FIGURE 9
Spatial distribution map of well locations and fault characteristics. **(a)** Well locations and fault plane distribution. **(b)** Cross-sectional view of 3D fault-architecture model.

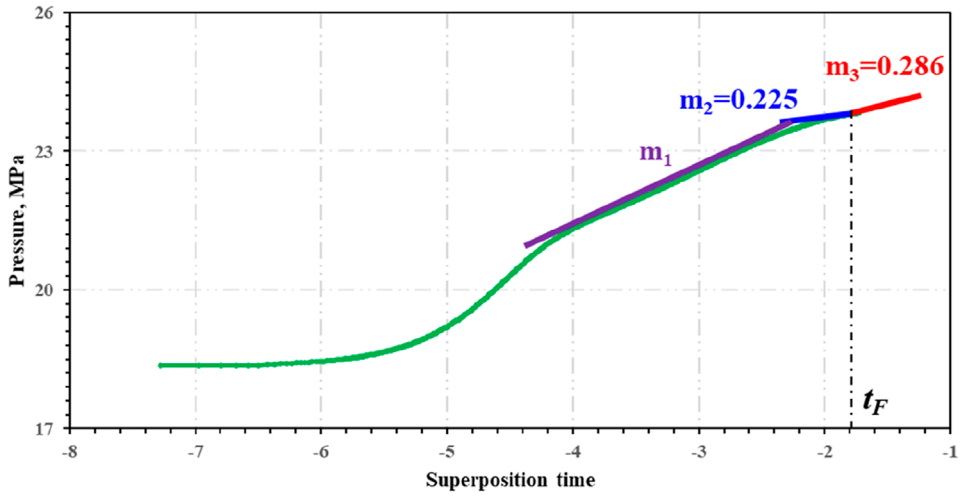

FIGURE 10
Semi-Log Well Test Curve Schematic of Bottomhole Flowing Pressure vs. Time for Well B1A.

as the fitness function, PSO iteratively updated particle positions to refine m_2 and m_3 estimates, ensuring convergence toward values more representative of the actual reservoir conditions.

To balance exploration efficiency and solution accuracy, the PSO algorithm employed a linearly decreasing inertia weight (from 0.9 to 0.4), with the maximum number of iterations set between 50 and 100 generations. During the training phase, five-fold cross-validation was incorporated to evaluate model generalization, and PSO was simultaneously utilized to perform automated hyperparameter tuning of the XGBoost model. This integrated modeling approach significantly enhanced the robustness and generalizability of the inversion results, demonstrating its effectiveness and practical value under complex fault-controlled reservoir conditions. As shown in Figure 10 are the inverted parameters m_2 and m_3.

As evidenced by the analysis of Figure 10, the semi-log curve of Well B1A exhibits characteristics consistent with an infinite-acting composite reservoir system. The initial slope m_1) corresponds to the formation properties of the inner zone, while the subsequent slope (m_2) reflects the characteristics of the outer zone. The third slope (m_3) clearly indicates the presence of a non-sealing fault boundary. Key reservoir parameters interpreted using our model include: inner zone permeability: 200 mD; composite radius: 220 m; outer zone permeability: 480 mD.

Figure 10 presents the pressure buildup test results from Well B1A conducted on 18 May 2013, where bottomhole flowing pressure was continuously monitored in real-time via a permanently installed downhole pressure gauge. Prior to shut-in, the well maintained an average production rate of 350 m^3/d. The semi-log pressure derivative curve demonstrates characteristic behavior during the outer boundary response phase, exhibiting an initial upward deflection followed by stabilization - a diagnostic pattern indicative of non-sealing fault influence. This confirms the presence of a fault boundary south of Well B1A. The inversion framework quantified two distinct pressure depletion rates: a second-stage slope (m_2) of 0.225 MPa representing the reservoir-dominated

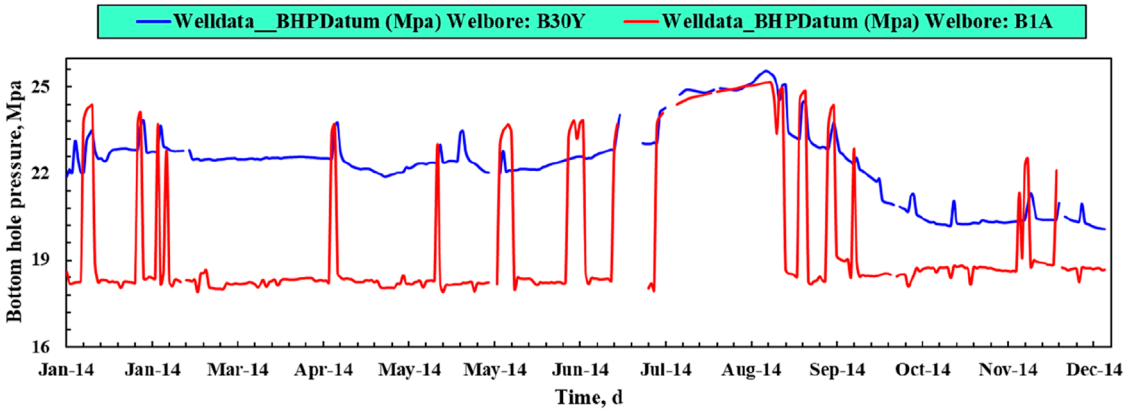

FIGURE 11
B1A and B30Y wellbore flow pressure variation curves.

flow regime, and a third-stage slope (m_3) of 0.286 MPa reflecting fault-affected flow. These inverted parameters (m_2 = 0.225, m_3 = 0.286) were subsequently input into Equations 46–49, yielding the fault's conductivity coefficient of 0.73 and effective connected thickness of 20.44 m.

$$\beta = \frac{m_3}{m_2} = 1.27 \tag{46}$$

$$C_F = (2-\beta)C_f = 0.73C_f \tag{47}$$

$$h_b = C_F\frac{\mu}{k_F} = (2-\beta)h = 20.44 \tag{48}$$

$$C_{fD} = \frac{C_F}{C_f} = 2-\beta = 0.73 \tag{49}$$

Previous geological architecture studies reveal that Fault *F1* connects thicker, high-quality sandstone units on its northern side with thinner but equally permeable sandstones to the south, exhibiting partial hydraulic communication. Analysis indicates that Fault *F1* has a geometric connectivity thickness of 0 m but an effective connected thickness of 24; Quantitative analysis demonstrates the fault's connectivity coefficient (C_{fD}) ranges between 0–1, with values trending closer to 1. This suggests that the fault is partially connected and has a high degree of connectivity, with a high degree of conductivity and a weak shading effect.

Based on this interpretation, development well B31Y was optimally positioned on the southern flank of Fault *F1*. After commissioning, the well achieved exceptional productivity of 2,000 cubic meters per day (m^3/d), demonstrating highly effective reservoir development.

Figure 11 displays the bottom hole pressure profiles for Wells B1A and B30Y throughout 2014, with particular emphasis on the pressure buildup test initiated on 29 July 2014. Prior to shut-in, the wells operated at distinct production rates: B30Y maintained a robust output averaging 2,400 m^3/d, while B1A produced at a more moderate rate of 480 m^3/d. Continuous BHP monitoring was facilitated by permanently installed downhole pressure gauges in both wells, providing real-time, high-resolution pressure data throughout the test sequence.

It can be seen from the figure that the bottomhole flow pressure of the shut-in wells B1A and B30Y has a similar change trend but is not exactly the same, which indicates that there is pressure conduction between the two wells, but there is a certain difference in the change trend due to the shielding effect of fault *F1*. It further proves that fault *F1* is a non-closed fault with strong pressure conduction ability, which verifies the reasonableness of the model calculation in this paper.

6 Conclusion

1. This study establishes a novel well-test interpretation model for composite reservoirs to characterize the limited conductivity of non-sealing faults. By incorporating the fluid flow mechanisms within fault zones into the analytical framework, the model significantly improves reservoir evaluation accuracy in the presence of conductive fault boundaries. The proposed approach provides new theoretical guidance and engineering methodologies for similar complex structural reservoirs.
2. A systematic analysis was conducted on the pressure and pressure derivative responses of composite reservoirs under varying fault conductivity and boundary distance conditions. The results demonstrate that non-sealing faults exhibit a diagnostic "upward deflection followed by stabilization" trend on the pressure derivative curve, serving as a key indicator for fault sealing evaluation. Additionally, the dimensionless derivative curve shows a strong positive correlation between the time of upward deflection and the fault boundary distance, providing a robust physical basis for quantitative inversion of fault location and sealing capacity.
3. An intelligent hybrid inversion framework (XGBoost-PSO) was developed and rigorously validated via a field case study in the *X* reservoir. Leveraging multi-stage pressure derivative characteristics and reservoir fluid properties, the inversion results quantitatively demonstrate that Fault *F1* functions as a partially conductive boundary, with its conductivity coefficient and effective connected thickness confirming significant fault connectivity. Bottom-hole pressure history matching during

the shut-in periods for Wells B1A and B30Y exhibits strong alignment with field monitoring data, validating the robustness and practical applicability of the proposed model and inversion framework. Future research should prioritize enhancing the model's generalizability to ensure broader deployment across diverse reservoir scenarios.

Data availability statement

The raw data supporting the conclusions of this article will be made available by the authors, without undue reservation.

Author contributions

YY: Methodology, Writing – review and editing. BL: Writing – original draft. XW: Formal Analysis, Writing – review and editing. MQ: Formal Analysis, Writing – review and editing. DZ: Data curation, Formal Analysis, Writing – review and editing.

Funding

The author(s) declare that financial support was received for the research and/or publication of this article. This research was funded by the National Science and Technology Major Project of China, grant number 2017ZX05009004-005 and National Natural Science Foundation of China, grant numbers 52074322, U1762210.

Conflict of interest

Authors YY, XW, MQ, and DZ were employed by CNOOC International Limited.

The remaining author declares that the research was conducted in the absence of any commercial or financial relationships that could be construed as a potential conflict of interest.

Generative AI statement

The author(s) declare that no Generative AI was used in the creation of this manuscript.

Any alternative text (alt text) provided alongside figures in this article has been generated by Frontiers with the support of artificial intelligence and reasonable efforts have been made to ensure accuracy, including review by the authors wherever possible. If you identify any issues, please contact us.

Publisher's note

References

Abdelaziz, B., and Tiab, D. (2004). "Pressure behavior of a well between two intersecting leaky faults," in Paper presented at the Canadian International Petroleum Conference, Calgary, Alberta. doi:10.2118/2004-209

Bixel, H. C., Larkin, B. K., and Van, H. K. (1963). Effect of linear discontinuities on pressure build-up and drawdown behavior. *J. Pet. Technol.* 15 (06), 885–895. doi:10.2118/611-PA

Dake, L. P. (1978). *Fumdamentals of reservoir engineering*. Elsevier Scientific Publishing Company.

Dong, P., and Liao, X. (2023). An efficient approach for automatic well-testing interpretation based on surrogate model and deep reinforcement learning. *Chin. J. Comput. Phys.* 40 (01), 67–80. doi:10.19596/j.cnki.1001-246x.8533

Fu, X., Lv, D., and Huang, J. (2022). Fault-caprock coupling sealing mechanism and fault trap hydrocarbon accumulation model. *Nat. Gas. Ind.* 42 (03), 21–28. doi:10.3787/j.issn.1000-0976.2022.03.003

Fu, X., Wang, H., and Song, X. (2024). Quantitative evaluation method and its application for vertical fault seal of thick caprock intervals. *Petroleum Geol. and Oilfield Dev. Daqing* 43 (04), 95–104. doi:10.19597/J.ISSN.1000-3754.202405013

Horner, D. R. (1951). *Pressure build-up in Wells 3rd world petroleum conference*. Netherlands: Society of Petroleum Engineers, 503–521.

Hu, X., Sandouhaxi, R., Liu, Y., and Lv, Y. (2024). Differences of lateral sealing ability between consequent fault and antithetic fault in Wen'an slope. *Chin. J. Geol.* 59 (4), 1057–1069. doi:10.12017/dzkx.2024.075

Kuchuk, F. J., and Tarek, H. (1997). Pressure behavior of laterally composite reservoir. *SPE Form. Eval.* 12 (1), 47–56. doi:10.2118/24678-PA

Li, X. (2023). *Research on automatic well test analysis method based on deep learning*. Anhui: Hefei University of Technology. doi:10.27101/d.cnki.ghfgu.2023.000182

Li, D., Liu, X., and Cha, W. (2020). Automatic well test interpretation based on convolutional neural network for a radial composite reservoir. *Petroleum Explor. Dev.* 47 (03), 583–591. doi:10.11698/PED.2020.03.14

Li, Y., Luo, L., and Wang, J. (2023). A geochemical evaluation method of fault sealing evolution and its controlling effect on hydrocarbon accumulation: a case study of the hongche fault zone in the northwest margin of the junggar basin. *Nat. Gas. Ind.* 43 (08), 12–25. doi:10.3787/j.issn.1000-0976.2023.08.002

Liu, H., Wang, G., and Wu, S. (2016). A study on pressure transmission of unsteady fluid flow in banded fault block reservoir. *J. Southwest Petroleum Univ. Sci. and Technol. Ed.* 38 (05), 135–142. doi:10.11885/issn-1674-5086.2014.08.26.02

Liu, Q., Jin, J., and Gui, F. (2017). Characteristics of well test curves corresponding to a combined reservoir with linear faults. *J. Southwest Petroleum Univ. Sci. and Technol. Ed.* 39 (04), 113–118. doi:10.11885/j.issn.1674-5086.2016.03.02.01

Liu, Y., Zhao, S., and Zhou, W. (2024). Dynamic evaluation model of fault sealing in water drive oilfield. *Fault-Block Oil and Gas Field* 31 (05), 877–884. doi:10.6056/dkyqt202405017

Ma, Q. (2025). Well test model of fractured well in linear shale oil reservoir with straight-line fault. *Complex Hydrocarb. Reserv.* 18 (01), 24–30. doi:10.16181/j.cnki.fzyqc.2025.01.004

Mi, L., Gu, S., and Xu, L. (2021). An intelligent well test interpretation method based on data driven technology: a case study from one water-producing gas well of water-bearing gas reservoirs. *Nat. Gas. Ind.* 41 (02), 119–124. doi:10.3787/j.issn.1000-0976.2021.02.014

Prasad, R. K. (1975). Pressure transient analysis in the presence of two intersecting boundaries. *J. Pet. Technol.* 27 (1), 89–96. doi:10.2118/4560-PA

Stewart, G., Gupta, A., and Westaway, P. (1984). "The interpretation of interference tests in a reservoir with a sealing and a partially communicating faults," in *Presented at the 1984 european petroleum conference*. London: Society of Petroleum Engineers, 411–429.

Streltsova, T. D., and McKinley, R. M. (1984). Effect of flow time duration on buildup pattern for reservoirs with heterogeneous properties. *SPEJ* 24 (3), 294–306. doi:10.2118/11140-PA

Wang, W., and Zhang, W. (1993). Application of semi logarithmic typical curve in well testing interpretation. *Well Test.* 2 (04), 42–46+50.

Xing, C., Yin, H., and Zhang, Y. (2023). Well test analysis model for ribbon-shaped composite reservoirs with partially permeable faults. *Petroleum Reserv. Eval. Dev.* 13 (02), 215–222. doi:10.13809/j.cnki.cn32-1825/te.2023.02.010

Yaxely, L. M. (1987). Effect of partially communicating fault on transient pressure behavior. *SPE Form. Eval.* 2 (4), 590–598. doi:10.2118/14311-PA

Zeng, Y., Wang, B., and Nie, R. (2017). The porous flow model of multi-stage fractured horizontal well in linear composite oil reservoirs. *Acta Pet. Sin.* 38 (06), 687–695. doi:10.7623/syxb201706008

Zhang, S. (2025). Application of pressure buildup test data in fine characterization of reservoirs in hade oilfield. *Well Test.* 34 (02), 73–78. doi:10.19680/j.cnki.1004-4388.2025.02.012